Observations of Time-Dependent Bedform Transformation in Combined Wave-Current Flows

Wengrove, M. E.; Foster, D. L.; Lippmann, T. C.; de Schipper, M. A.; Calantoni, J.

DOI
10.1029/2018JC014357

Publication date
2018

Document Version
Final published version

Published in
Journal of Geophysical Research: Oceans

Citation (APA)
Wengrove, M. E., Foster, D. L., Lippmann, T. C., de Schipper, M. A., & Calantoni, J. (2018). Observations of Time-Dependent Bedform Transformation in Combined Wave-Current Flows. *Journal of Geophysical Research: Oceans*, *123*(10), 7581-7598. https://doi.org/10.1029/2018JC014357

Journal of Geophysical Research: Oceans

RESEARCH ARTICLE
10.1029/2018JC014357

Observations of Time-Dependent Bedform Transformation in Combined Wave-Current Flows

M. E. Wengrove[1], D. L. Foster[2], T. C. Lippmann[3], M. A. de Schipper[4], and J. Calantoni[5]

[1]School of Civil and Construction, Oregon State University, Corvallis, OR, USA, [2]Department of Mechanical and Ocean Engineering, University of New Hampshire, Durham, NH, USA, [3]Earth Sciences and Center of Coastal and Ocean Mapping, University of New Hampshire, Durham, NH, USA, [4]Hydraulic Engineering, Delft University of Technology, Delft, Netherlands, [5]Marine Geosciences Division, U.S. Naval Research Laboratory, Stennis, MS, USA

Key Points:
- Bedform building is a time-dependent process especially important in combined wave-current flows
- The sediment continuity equation or Exner equation can be used to estimate bedform volume change
- Contribution of unique data set of combined waves and current influence on bottom roughness

Correspondence to:
M. E. Wengrove,
meagan.wengrove@oregonstate.edu

Citation:
Wengrove, M. E., Foster, D. L., Lippmann, T. C., de Schipper, M. A., & Calantoni, J. (2018). Observations of time-dependent bedform transformation in combined wave-current flows. *Journal of Geophysical Research: Oceans*, *123*. https://doi.org/10.1029/2018JC014357

Received 17 JAN 2018
Accepted 30 SEP 2018
Accepted article online 8 OCT 2018

Abstract Although combined wave-current flows in the nearshore coastal zone are common, there are few observations of bedform response and inherent geometric scaling in combined flows. Our effort presents observations of bedform dynamics that were strongly influenced by waves, currents, and combined wave-current flow at two sampling locations separated by 60 m in the cross shore. Observations were collected in 2014 at the Sand Engine mega-nourishment on the Delfland coast of the Netherlands. The bedforms had wavelengths ranging from 14 cm to over 2 m and transformed shape and orientation within, at times, as little as 20 min and up to 6 hr. The dynamic set of observations was used to evaluate a fully unsteady description of changes in the bedform growth with the sediment transport continuity equation (Exner equation), relating changes in bedform volume to bedload sediment transport. Analysis shows that bedform volume was a function of the integrated transport rate over the bedform development time period. The bedform development time period (time lag of bedform growth/adjustment) is important for estimating changes in bedform volume. Results show that this continuity principle held for wave, current, and combined wave-current generated bedforms.

Plain Language Summary Just under the water at sandy beaches around the world there are sand ripples that form, grow, move, change, and decay. While the ripple feature is very aesthetically pleasing, it also serves the purpose of moving sand toward and away from the coast. In order for us to accurately predict coastal change, it is important to fully understand how sand ripples grow and decay in waves, currents, and combined wave-current flows. Field observations of growing and changing sand ripples in combined wave-current flows are used to validate a new analytical expression for estimating bedform growth and decay due to changes in the flow field energy.

1. Introduction

Time-varying wave, current, and combined wave-current flows are characteristic of most nearshore regions (e.g., Grant & Madsen, 1979; Passchier & Kleinhans, 2005; Soulsby & Clarke, 2005). These complex hydrodynamic environments are complicated with small scale bed roughness (e.g., sand ripples and megaripples) that have a two-way feedback with the local hydrodynamics, apparent within nearshore modeling (Ganju & Sherwood, 2010; Lesser et al., 2004; Wikramanayake & Madsen, 1994). Previous research demonstrates that characteristic bedform roughness lengths (bedform wavelength and height) scale with the sediment particle size and the hydrodynamic forcing applied to the seabed under waves or currents (e.g., Clifton & Dingler, 1984; Fredsøe, 1984; Hay & Mudg, 2005; Traykovski et al., 1999; Wiberg & Harris, 1994). However, there have been very few studies of bedform scaling and orientation in response to dynamically changing forcing that includes combined wave-current flows (Hay & Mudg, 2005; Lacy et al., 2007; Li & Amos, 1998; Nelson & Voulgaris, 2015; Soulsby et al., 2012).

For combined wave-current flows, most of the literature addresses the transition of bedforms between flow states with observations of relatively small bedforms with wavelengths of less than 0.5 m under relatively low energy wave conditions or with waves plus weak mean flow (e.g., Grant & Madsen, 1979; Lacy et al., 2007; Li & Amos, 1998; Soulsby & Clarke, 2005; Soulsby et al., 2012). Results of these efforts show that combined flow bedforms are less steep than wave dominant bedforms and generally orient in a pattern influenced by the maximum gross bedform normal transport direction (Gallagher et al., 1998; Lacy et al., 2007). There are

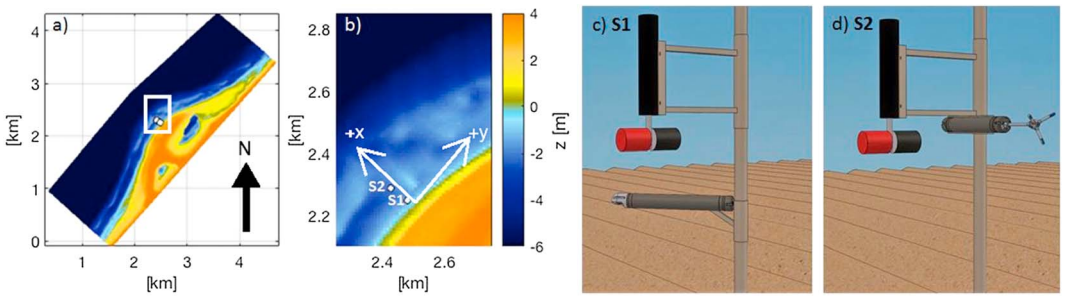

Figure 1. (a) September 2014 bathymetry of Sand Engine mega-nourishment, Delfland, the Netherlands. (b) Inset marked on panel (a) shows the sampling locations S1 and S2 indicated with white circles. Site S1 is close to the shoreline, and site S2 is close to the shore-parallel sandbar. The coordinate system used in this research is defined relative to the low-tide shoreline, where shore parallel (alongshore) is *y* with *+y* being toward the northeast, and shore normal (cross shore) is *x* with *+x* directed offshore. (c and d) Instrument array. Station S1 included an Imagenex 881a pencil beam sonar located 0.7 m from the bed and an acoustic Doppler current profiler located 0.4 m from the bed, and station S2 included an Imagenex 881a pencil beam sonar 1 m from the bed and an acoustic Doppler velocimeter 1 m from the bed.

a limited number efforts that observe larger-scale bedforms, like megaripples, in wave dominant or combined flows (Gallagher, 2003; Gallagher et al., 1998; Larsen et al., 2015), but these efforts do not address characteristics of bedform response to transition periods.

Observations of bedforms under wave dominant or current dominant flows suggests that bedform building is a time-dependent process (e.g., Austin et al., 2007; Davis et al., 2004; Doucette & O'Donoghue, 2006; Nelson & Voulgaris, 2015; Soulsby et al., 2012; Testik et al., 2005; Traykovski, 2007). The bedform shape and volume is dependent on present hydrodynamic conditions, as well as past forcing. Time-dependent bedform models that estimate roughness length scales use a departure from equilibrium approach (e.g., Soulsby et al., 2012; Traykovski, 2007) that assumes bedform length scales are being driven toward equilibrium with the present hydrodynamic conditions. The assumption is generally valid for waves (Davis et al., 2004; Doucette & O'Donoghue, 2006; Testik et al., 2005; Traykovski, 2007); however, present equilibrium theory may not capture the physics of bedform adjustment in combined wave-current flows because the time constants associated with current models may not be appropriate to represent dynamics in combined flows (Austin et al., 2007).

In our effort, we present observations of ripple and megaripple formation in response to high-energy combined flows with, at times, the addition of a strong current. Forcing conditions ranged from wave dominant flow, to combined wave-current flow, to mean current flow. Bedform transition periods and growth cycles were observed in response to the variable flow conditions. Additionally, the results demonstrate that the sediment continuity equation, or Exner equation, captures bedform building as a time-dependent process, suggesting that the sediment continuity equation may be used to model dynamic roughness in the nearshore, especially relevant when considering combined wave-current flows.

2. Methods

2.1. Experiment and Instrumentation

Data were collected during a field campaign at the Sand Engine mega-nourishment as a part of the MEGA-Perturbation EXperiment in the fall of 2014 on the Delfland Coast of the Netherlands (Radermacher et al., 2017). Since the installment of the 21.5 million cubic meters of sand in 2011, the Sand Engine has dramatically changed shape (Stive et al., 2013); in 2011 it stretched 2 km in the alongshore and 1 km into the North Sea, and in 2014 it stretched 4 km alongshore and 800 m in the cross shore (Radermacher et al., 2017). The large-scale morphology is considered very dynamic with observable bathymetric changes over periods of days to months. Our effort investigates the dynamic nature of the small scale morphology at the seaward tip of the Sand Engine.

Local small-scale morphology and hydrodynamics were observed between the shoreline and the shore-parallel sandbar that were 136 m apart at two cross shore stations, S1 and S2, at the tip of the Sand Engine (Figure 1a). S1 was located 20 m seaward of the low-tide shoreline, and S2 was located 66 m further offshore and 50 m shoreward of the subtidal sandbar. Morphology was sampled at each location with a stationary sweeping and rotating 1-MHz Imagenex 881a pencil beam sonar with a 3-m diameter footprint. S1 was sampled every 20 min with a 1.4° sweep step and a 2.4° rotation step from 26 September to 23 October

2014 (day of year 269–296), and S2 was sampled every 2 hr with a 1.4° sweep step and a 1.4° rotation step from 2 to 18 October (day of year 275 to 291). Hydrodynamic forcing was measured at S1 using a downward looking high-resolution acoustic Doppler current profiler positioned 0.4 m above the seabed and burst sampled for 20 min every hour at 4 Hz, and at S2 using an acoustic Doppler velocimeter positioned 1 m above the seabed and burst sampled for 20 min every hour at 64 Hz (Figure 1b). The mean lower low water depth at S1 was −1.0-m Normaal Amsterdam Peil (approximately mean sea level) and at S2 was −1.7-m Normaal Amsterdam Peil, and the median sediment grain size of the quartz sediment at both sites was 350 μm. The tidal range was approximately 1.5 m. Large-scale bathymetry was measured with an echo sounder during regular jet ski surveys. The large-scale coordinate system used throughout this paper is with respect to degrees from shore normal, with 0° being onshore (−x), +90° rotating counterclockwise from shore normal, and −90° rotating clockwise from shore normal.

2.2. Hydrodynamics

The local flow at each monitoring station was decomposed into current velocities, with magnitude U and direction ϕ_c, and wave orbital velocities, with magnitude u_o and direction ϕ_w, over 10-min-averaged time intervals. The current velocity is defined by the resultant of the temporal mean of the horizontal (u, v) velocities with

$$U = |\bar{u}|, \tag{1}$$

and the overbar represents a temporal average over 10 min. The magnitude of the orbital velocity assumes a sinusoidal velocity with

$$u_o = \sqrt{2}u_{\text{std}}, \tag{2}$$

where $u_{\text{std}} = \overline{[(u-U)^2]^{0.5}}$ (Traykovski et al., 1999). The current and wave velocities were either measured directly at 10 cm above the bedform crest or calculated using a log layer approximation for the mean flow contribution and linear wave theory for the wave contribution to 10 cm above the bedform crest. The 10 cm measurement or attenuated estimation of current and wave velocities is used for all subsequent analysis and in all figures.

The wave period is defined with

$$T = \frac{2\pi}{S_{m_2}/S_{m_1}}, \tag{3}$$

where S is the spectra of the pressure signal and the subscripts m_1 and m_2 refer to the first (mean) and second (variance) moments of the spectra (Madsen et al., 1988). The wave orbital diameter was defined with

$$d_o = 2\frac{u_o}{2\pi/T}. \tag{4}$$

The combined wave-current velocity (Lacy et al., 2007) relates the wave orbital and current velocities with a third term representing the combined effect depending on the angle between the orbital and current velocities, where

$$u_{\text{wc}} = \left[u_o^2 + U^2 + 2u_o U\cos|\phi_w - \phi_c|\right]^{0.5}. \tag{5}$$

Finally, the maximum kinetic energy in the combined wave-current flows is defined as

$$E_{k_{\text{wc}}} = \frac{1}{2}u_{\text{wc}}^2. \tag{6}$$

In our observations we distinguish between wave dominant, current dominant, and combined flow conditions using a fraction-of-energy approach to assess the contribution of waves and/or currents to sediment flux. $E_{k_{\text{wc}}}$ is defined as the maximum kinetic energy in the flow field including both waves and currents. $E_{k_w}/E_{k_{\text{wc}}}$ is defined as the fraction of kinetic energy due to waves. A value of 1 would be purely wave driven flow, and a value of 0 would be purely current driven flow. Previous literature has distinguished wave dominant flows from combined flows based on a ratio of wave induced to current induced friction velocity, where purely wave ripples occur at a friction velocity ratio of 0.5 or greater (Lacy et al., 2007; Li & Amos, 1998). The estimate of friction velocity can vary widely based upon the method used to estimate the bed shear stress (particularly when the bedform field is highly dynamic), where $u_* = (\tau_b/\rho)^{1/2}$. So u_* was not used to evaluate the relative strength of the waves and currents. Rather, we chose to express the relative strength of waves and currents as a function of the total kinetic energy. To put the limit from Lacy et al. (2007) in terms of energy, the threshold of 0.5 is squared. Such that we define $E_{k_w}/E_{k_{\text{wc}}} > 0.75$ to be wave dominant, $0.75 \geq E_{k_w}/E_{k_{\text{wc}}} \geq 0.25$ for combined wave-current flow, and $0.25 > E_{k_w}/E_{k_{\text{wc}}}$ to be current dominant.

2.3. Measured Bedform Statistics

Statistics of bedform wavelength (λ), bedform height (η), and bedform orientation (ϕ_r) are determined through analysis of sonar return data. Bottom position within each sonar data set was found by identifying the high-intensity return region for each sonar ping using two methods. The first is a weighted mean sum (WMS) method, and the second is a bearing direction indicator (BDI) method (SeaBeam, 2000). WMS applies a weighted mean sum to each sonar ping, where the location of the highest WMS for each beam is the location of the bed. The WMS method works well for return data with high grazing angles (data within 30° of the sonar nadir). The BDI applies a parabolic fit to the high-intensity return for all the beams intersecting the same section of bed within one sweep over multiple pings. The BDI method is suited to intensity returns at low grazing angles since the multiple ping fit gives higher confidence in bed location. WMS was used to detect the bed within the inner 1-m diameter at bed level, and BDI was used to detect the bed from the 1-m diameter range to the sonar sampling extent at bed level (see ; Wengrove et al., 2017, for more details).

With a time series of 2-D local bathymetries (Figures 2f–2h and 3f–3h), the dominant ripple wavelengths, heights, and orientations were determined with normalized 2-D spatial wavenumber spectral analysis (Becker et al., 2007; Maier & Hay, 2009). The 2-D spatial spectra, S (m^3), have axes of wavenumber, k_x (cross shore), and k_y (alongshore) (1/m). The spectra were normalized by premultiplying S by the wavenumber k_x and k_y, where $\hat{S} = Sk_xk_y$ (Alamo & Jimenez, 2003). The benefit of a normalized spectra is that the multiplication by wavenumber emphasizes higher wavenumbers and enhances the energy peaks of interest for analysis. The energy distribution in the spectra indicate the dominant bedform wave number and orientation. The bedform wavelength is defined as the bedform normal distance from crest to crest, and the bedform height is defined as the vertical distance between bedform trough and crest. Estimates of bedform height are found by integrating the spectrum, analogous to a significant ocean wave height calculation from temporal spectral analysis (Penko et al., 2017; Traykovski, 2007; see ; Wengrove et al., 2017, for more details).

The lower limit of uncertainties associated with the spatial resolution of the pencil beam sonar measurements were related to range resolution, beam width, and sweep and rotation step angles. During the course of the experiment the water temperature stayed relatively constant with time, and a sound speed of 1,502 m/s was used to convert sonar time returns into range estimates. The range resolution of the pencil beam is 2 mm for a sampling range of 1 to 4 m. The conical beam width operating at 1 MHz is 1.4°, so 1 m away from the transducer (within 30° of the sonar nadir) the resolution limit is 2.5 cm, while at the profiling extent or approximately 2 m way from the transducer, the resolution limit becomes 5.0 cm. Finally, with respect to spatial sampling step angle, for S1, directly under the sonar the spatial resolution was 2 cm × 4 cm and at the radial edge of the swath the spatial resolution was 5 cm × 8 cm. For S2, directly under the sonar the spatial resolution was 2 cm × 2 cm and at the profiling extent the spatial resolution was 5 cm × 5 cm. With these limitations, the smallest bedform wavelength that could be resolved within the inner 30° of the sonar nadir was approximately 12 cm, and at the profiling extent was approximately 25 cm. Bedform height could be resolved within 2 cm. The profiling extent of the pencil beam sonar was 3 m in diameter.

The largest bedform wavelength that was measured during the experiment was just under 3 m. Any bedforms that were larger than 1.5 m in wavelength had only one to two wavelengths visible in the field of view of the sonar. In these cases, the 2-D sonar field of view was beneficial to not only measure bedform orientation but to give greater confidence to the measurement of bedform wavelength. Within the sonar field of view, there were >50 measurements (effectively ensembles) of the bedform wavelength perpendicular to the bedform crest. Bedforms with wavelengths of greater than 3 m could not be resolved, which is an inherent limitation of the data set; however, there were no evidence for the presence of larger wavelength bedforms during the experiment (e.g., a sloped boundary within the sonar field of view), and jet ski surveys did not show evidence of much larger wavelength bedforms (> 20 m) in the local area.

Bedform migration magnitude was estimated using subsequent local 2-D bathymetric pairs from the pencil beam sonar. Each pair of bathymetries was processed with either a 2-D cross correlation as defined in Wengrove et al. (2017) or a motion estimator process (MEP) least squares error approach (Perkovic et al., 2009). The 2-D cross correlation is a measure of similarity of the two bathymetries based on the displacement of one relative to the other, highlighting shifts (or bedform migrations) between bathymetries (similar to techniques used in Particle Image Velocimetry). If there are bedforms with multiple wavelengths within the sonar view window then the 2-D cross-correlation method works well. However, when the bedforms get large, there may only be one wavelength in view; in this case, the MEP method is a more robust method because the least

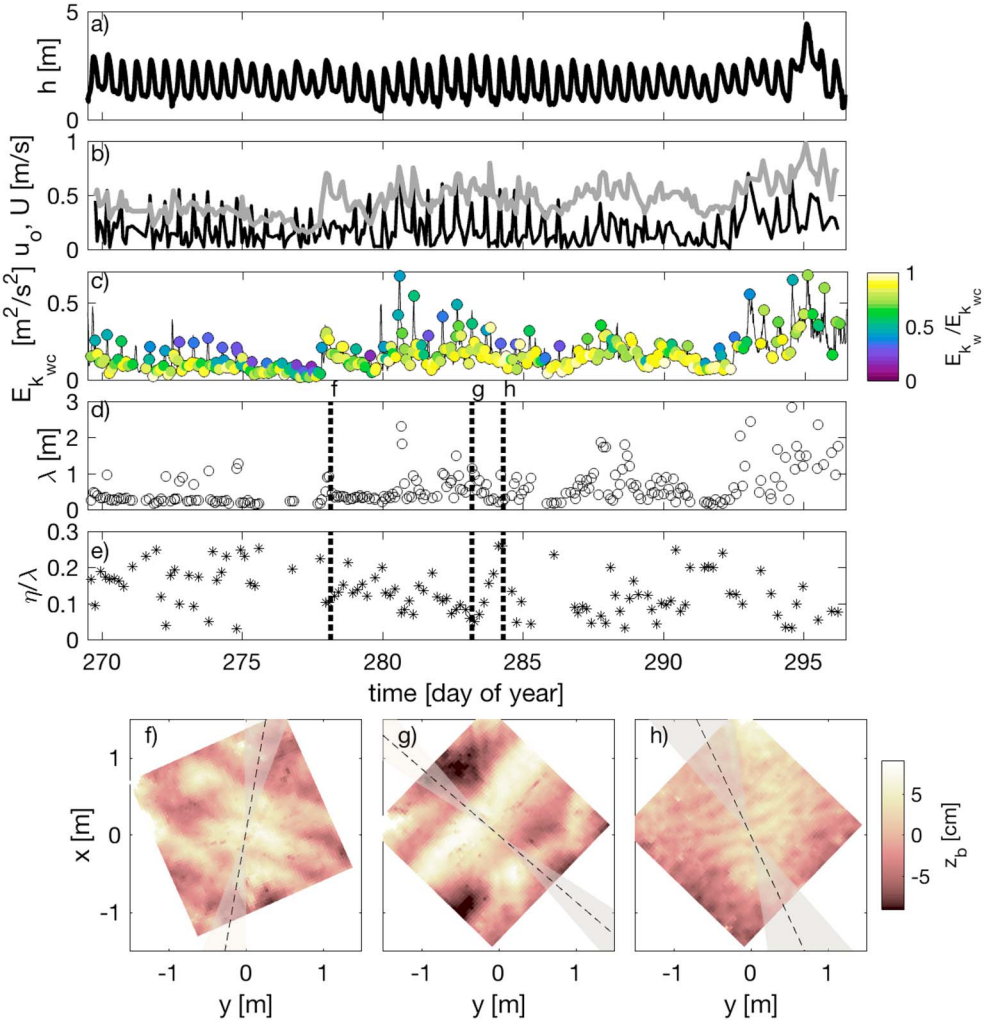

Figure 2. Time series of observations at S1, where panel (a) shows depth (h); (b) shows amplitude of wave orbital velocity, u_o, in gray and mean velocity, U, in black; (c) shows maximum kinetic energy, $E_{k_{wc}}$ shaded by fraction of kinetic energy due to waves; (d) shows ripple wavelength, λ; and (e) shows ripple steepness, η/λ. The vertical dashed lines in panels (d) and (e) indicate occurrences of local bathymetries shown as panels (f)–(h). Panels (f)–(h) show 2-D bathymetries, where y is shore parallel and x is shore normal, with $-x$ directed onshore, and is shaded by bedform height. Finally, dashed lines and shaded overlay in panels (f)–(h) indicate bedform orientation and orientation uncertainty, respectively.

squares analysis is much less sensitive for smaller viewing windows relative to bedform wavelength. Once the bedform displacement, $d_{xy} = (d_x^2 + d_y^2)^{0.5}$, was found between each subsequent bathymetric pair, the bedform migration rate was found by $V_{\text{mig.}} = d_{xy}/t_s$, where t_s is the sampling time between bathymetric pairs (Wengrove et al., 2017).

Uncertainties associated with the temporal resolution of the bedform migration involve the time scale for the sonar sensor rotations. Bedload sediment transport processes with a time scale less than a full sweep rotation time window were not resolved; for S1 this was 10 min, and for S2 this was 15 min. Additionally, processes that occurred with a time scale of less than the time between subsequent sonar scans, dt, were not resolved; dt was 20 min for S1 and 2 hr for S2. However, the low noise floor of the spectra of the time series of observed bedform wavelengths over the month long deployment at S1 showed that there were no sign of aliasing with a dt of 20 min for estimating migration rates (not shown), so a dt of 15 min to estimate migration rates at S2 is considered sufficient as well.

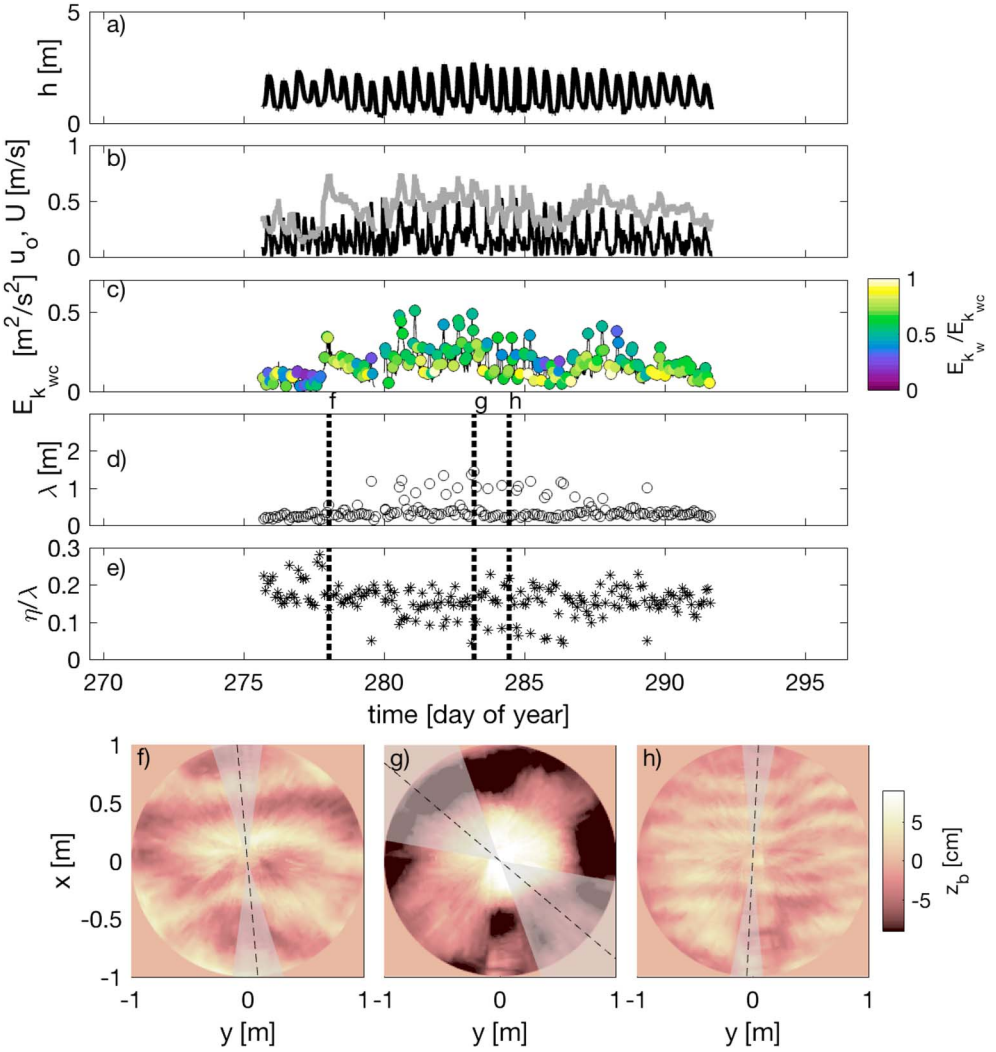

Figure 3. Time series of observations at S2, where panel (a) shows depth (h); (b) shows amplitude of wave orbital velocity, u_o, in gray and mean velocity, U, in black; (c) shows maximum kinetic energy, $E_{k_{wc}}$ shaded by fraction of kinetic energy due to waves; (d) shows ripple wavelength, λ; and (e) shows ripple steepness, η/λ. The vertical dashed lines in panels (d) and (e) indicate occurrences of local bathymetries shown as panels (f)–(h). Panels (f)–(h) show 2-D bathymetries, where y is shore parallel and x is shore normal, with $-x$ directed onshore, and is shaded by bedform height. Finally, dashed lines and shaded overlay in panels (f)–(h) indicate bedform orientation and orientation uncertainty, respectively.

2.4. Sediment Continuity Equation

Assuming a sinusoidal function for transport,

$$\mathbf{q_b} = q_b \cos\left[\frac{2\pi}{\lambda}\left(V_{\text{mig.}}t - x_b - \delta_{x_b}\right)\right], \tag{7}$$

where $\mathbf{q_b}$ is the bedload sediment flux ($m^3 \cdot m \cdot s$), q_b is the scalar transport, $V_{\text{mig.}}$ is the migration rate, t is time, λ is the wave length, δ_{x_b} is the phase offset between the bedform shape and the function for transport, x_b is the position along the bedform wavelength, and t is time. Using $\cos(\alpha - \beta) = \cos(\alpha)\cos(\beta) + \sin(\alpha)\sin(\beta)$,

$$q_b = q_1 \cos\left[\frac{2\pi}{\lambda}\left(V_{\text{mig.}}t - x_b\right)\right] + q_2 \sin\left[\frac{2\pi}{\lambda}\left(V_{\text{mig.}}t - x_b\right)\right], \tag{8}$$

$$q_1 = q_b \cos\left(\frac{2\pi}{\lambda}\delta_{x_b}\right), q_2 = q_b \sin\left(\frac{2\pi}{\lambda}\delta_{x_b}\right), \tag{9}$$

and $q_2/q_1 = \tan(\frac{2\pi}{\lambda}\delta_{x_b})$. We assume the bed level, z_b, as

$$z_b(x,t) = \eta \cos\left[\frac{2\pi}{\lambda}\left(V_{\text{mig.}}t - x_b\right)\right]. \tag{10}$$

where η is the amplitude of the bedform. The bedform height, wavelength, and migration rate are allowed to be fully unsteady.

The sediment continuity equation, or the Exner equation, relates the sediment flux gradient per unit width to the rate of bed level change (Nielsen, 1992) and is commonly expressed with

$$\frac{\partial q_b}{\partial x} \equiv -n\frac{\partial z_b}{\partial t}. \tag{11}$$

where n is the sediment packing (~ 0.7 for sand). For the case of bedform migration or transformation with no local accretion or erosion, the bed elevation, z_b, can be expressed by the local bedform geometry ($z_b = \eta$). By taking the spatial derivative of the expression for q_b and the temporal derivative of the expression for z_b, and assuming that η, λ, and $V_{\text{mig.}}$ are a function of t, but q_1 and q_2 are not a function of x, then

$$\frac{\partial q_b}{\partial x} = q_1\frac{2\pi}{\lambda}\sin\left[\frac{2\pi}{\lambda}\left(V_{\text{mig.}}t - x_b\right)\right] - q_2\frac{2\pi}{\lambda}\cos\left[\frac{2\pi}{\lambda}\left(V_{\text{mig.}}t - x_b\right)\right] \tag{12}$$

and

$$\frac{\partial z_b}{\partial t} = \frac{\partial \eta}{\partial t}\cos\left[\frac{2\pi}{\lambda}\left(V_{\text{mig.}}t - x\right)\right] - \eta\left[2\pi\left(\frac{t}{\lambda}\frac{\partial V_{\text{mig.}}}{\partial t} + V_{\text{mig.}}t\frac{\partial}{\partial t}\frac{1}{\lambda} + \frac{V_{\text{mig.}}}{\lambda} - x_b\frac{\partial}{\partial t}\frac{1}{\lambda}\right)\right]\sin\left[\frac{2\pi}{\lambda}\left(V_{\text{mig.}}t - x\right)\right]. \tag{13}$$

Now, using (12) and (13) in (11) and the definition if $ax + by = mx + ny$ then $a = m$ and $b = n$ shows that

$$n\eta\left[2\pi\left(\frac{t}{\lambda}\frac{\partial V_{\text{mig.}}}{\partial t} + V_{\text{mig.}}t\frac{\partial}{\partial t}\frac{1}{\lambda} + \frac{V_{\text{mig.}}}{\lambda} - x_b\frac{\partial}{\partial t}\frac{1}{\lambda}\right)\right] = \frac{2\pi}{\lambda}q_1, \tag{14}$$

and

$$n\frac{\partial \eta}{\partial t} = \frac{2\pi}{\lambda}q_2 \tag{15}$$

where (14) represents the unsteady sediment flux from the migrating bedform and (15) represents the unsteady sediment flux from a growing or decaying bedform. Expressions for the bedform migration and growth with a semisteady assumption for the bedform λ and $V_{\text{mig.}}$ can be found in Nielsen (1992) and Roelvink and Reniers (2011). Both (14) and (15) are theoretically equivalent, by substituting (9) into (14) and (15) and equating the result by means of q_b gives

$$\frac{\partial \eta}{\partial t} = 2\pi\eta\left(\frac{t}{\lambda}\frac{\partial V_{\text{mig.}}}{\partial t} + V_{\text{mig.}}t\frac{\partial}{\partial t}\frac{1}{\lambda} + \frac{V_{\text{mig.}}}{\lambda} - x_b\frac{\partial}{\partial t}\frac{1}{\lambda}\right)\tan\left(\frac{2\pi}{\lambda}\delta_{x_b}\right). \tag{16}$$

An expression for δ_{x_b}/λ as a function of $\partial\eta/\partial t$ and $V_{\text{mig.}}$ follows

$$\delta_{x_b}/\lambda = \frac{1}{2\pi}\tan^{-1}\left[\frac{\partial \eta}{\partial t}\Big/\left(2\pi\eta\left(\frac{t}{\lambda}\frac{\partial V_{\text{mig.}}}{\partial t} + V_{\text{mig.}}t\frac{\partial}{\partial t}\frac{1}{\lambda} + \frac{V_{\text{mig.}}}{\lambda} - x_b\frac{\partial}{\partial t}\frac{1}{\lambda}\right)\right)\right]. \tag{17}$$

The bedform volumetric change as a function of the sediment flux is found beginning with (15) and expanding the time rate of change in bedform height with the product rule

$$\frac{n\lambda}{2\pi}\frac{\partial \eta}{\partial t} = \frac{n}{2\pi}\frac{\partial \eta\lambda}{\partial t} - \frac{n}{2\pi}\frac{\eta\partial\lambda}{\partial t}. \tag{18}$$

By substituting the expression for q_2 and integrating the manipulation from $t - \tau$ to τ, an expression for the bedform volumetric change is given as

$$\Delta\Lambda_b = \Delta\frac{n}{2}\eta\lambda = \int_{t-\tau}^{t}\pi q_b \sin\left(2\pi\delta_{x_b}/\lambda\right)\mathrm{d}t + \int_{t-\tau}^{t}\frac{n}{2}\frac{\eta\partial\lambda}{\partial t}\mathrm{d}t. \tag{19}$$

where $\Delta\frac{n}{2}\eta\lambda$ is the change in volume of the bedform, $\Delta\Lambda_b$, over some time since it started to grow or decay, $\tau - t$, to the present time, t. The first term on the right-hand side is the portion of the time-integrated sediment flux related to bedform growth or decay. The second term on the right-hand side of (19) is related to the bedform stretching over time. The expression represents a fully unsteady derivation of bedform transformation and translation with respect to bedform height, wavelength, and migration.

2.5. Existing Time-Dependent Bedform Geometry Models

In laboratory settings Davis et al. (2004), Smith and Sleath (2005), Testik et al. (2005), and Doucette and O'Donoghue (2006) explored the time-dependent nature of bedforms between equilibrium conditions, as well as the associated time scale for bedforms to reach an asymptotic equilibrium state with imposed wave forcing conditions. These studies give estimates for bedform temporal adjustment to equilibrium based on sediment transport rates, with each showing that it takes time for bedforms to evolve and grow between equilibrium states. In field settings, Traykovski (2007), Soulsby et al. (2012), and Nelson and Voulgaris (2015) also take a departure from equilibrium approach by relating a change in geometry over a period of time to a departure from equilibrium geometry model that imposes a parameterized time scale of change. Our effort further considers the wave-only spectral time-dependent model of Traykovski (2007), and the wave or current dominant time-dependent model of Soulsby et al. (2012); each summarized in the following.

Bedform evolution can be characterized with a time-varying spectrum of bedform geometries defined by (Traykovski, 2007)

$$\frac{\mathrm{d}\eta_{T07}(k)}{\mathrm{d}t} = \frac{\eta_{\mathrm{eq}}(k) - \eta_{T07}(k)}{T_{\mathrm{adj}}(k)}, \tag{20}$$

where k is the associated bedform wavenumber ($2\pi/\lambda$), η_{eq} is the equilibrium ripple spectra modeled by a Gaussian distribution with inputs of a proposed equilibrium ripple height and ripple wavelength, and $T_{\mathrm{adj}}(k)$ is an adjustment time scale for each wavenumber based on the wavenumber-dependent cross-sectional area of the bedform and the total bedform sediment flux, q (Meyer-Peter & Muller, 1948). A numerical integration scheme results in a time series of wavenumber-dependent ripple heights, where modeled $\eta_{m_{T07}}$ is found by integrating with respect to wavenumber (analogous to a significant wave height calculation) as discussed previously, and modeled $\lambda_{m_{T07}}$ is defined by $2\pi/k$ of the peak spectral energy band for each time step. The model gives high-skill predictions of ripple geometry in a predominantly wave environment, where the model skill is the correlation coefficient squared.

Soulsby et al. (2012) proposed a time-dependent bedform evolution model that uses a Shields parameter criterion to decide whether ripples are wave or current generated. A departure from equilibrium approach allows ripples to evolve based on an adjustment time scale. For a given bedform variable (either ripple wavelength or height) the model is defined by

$$\frac{\mathrm{d}x_{\mathrm{SWM12}}}{\mathrm{d}t} = a(t) - b(t)x_{\mathrm{SWM12}}(t), \tag{21}$$

where x_{SWM12} is either the modeled $\eta_{m_{\mathrm{SWM12}}}$ or $\lambda_{m_{\mathrm{SWM12}}}$ and is found through numerical integration. Additionally, $a(t) = x_{\mathrm{eq}}\beta/T_r$ and $b(t) = \beta/T_r + bio/T_b$, where x_{eq} is an equilibrium length and β is a rate of change parameter based on waves or current dominant forcing. T_r is a rate of change characteristic time scale that is equal to the wave period for wave forcing conditions and the time taken for an equilibrium ripple to be changed by the total bedload transport rate for current forcing. bio and T_b are a free parameter and a time scale related to biological degradation of the bedforms, respectively. The model has been shown to have high skill in prediction of wave dominant flow or current dominant flow bedforms of less than 0.5 m in wavelength; however, it does not predict megaripples and does not account for combined wave-current flows.

3. Results

3.1. Observations of Bedform Geometry

Time series of hydrodynamic and bedform geometry observations are shown in Figures 2 and 3 for S1 and S2, respectively. S1 was deployed for a spring-neap-spring-neap-spring tidal cycle, including four storm events (day of year 278, 280, 287, and 294). S2 was deployed for a neap-spring-neap tidal cycle with three storm events (day of year 278, 280, and 287). At both locations the currents were strongly tidally influenced with stronger currents during flood tide, as the tidal flow runs parallel to the Delfland coast. Additionally, wave orbital velocities were tidally modulated due to waves breaking on an shore-parallel sandbar during low water, and more shoreward during high water (see Figure 1).

Bedform geometry was observed to vary substantially at each station over the period of investigation with a clear dependence on the type of hydrodynamic forcing (Figures 2 and 3). The hydrodynamic kinetic energy shaded by the fraction of energy due to waves $\left(E_{k_w}/E_{k_{\mathrm{wc}}}\right)$ highlights occurrences of current-dominated flows $\left(\text{low } E_{k_w}/E_{k_{\mathrm{wc}}}\right)$ and wave-dominated flows $\left(\text{high } E_{k_w}/E_{k_{\mathrm{wc}}}\right)$. Current dominant flows occurred only 2% of the

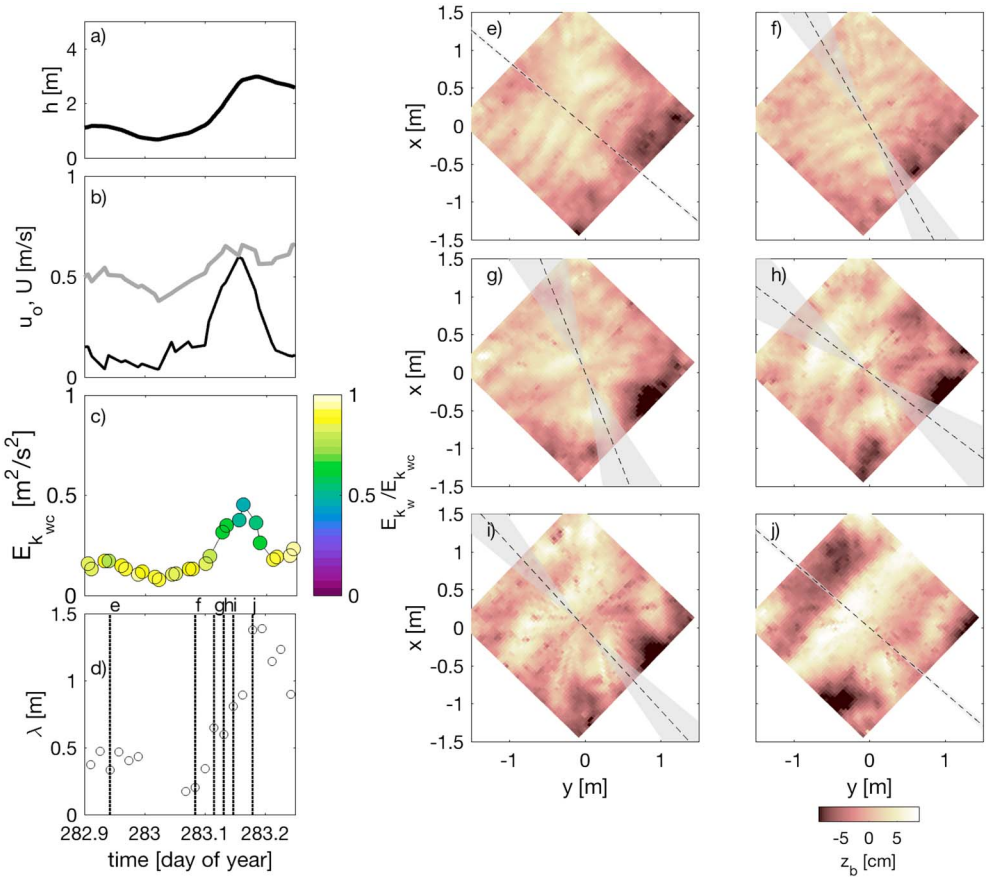

Figure 4. Time series of observations at S1 for one tidal cycle, where panel (a) shows depth (h); (b) shows amplitude of wave orbital velocity, u_o, in gray and mean velocity, U, in black; (c) shows maximum kinetic energy, $E_{k_{wc}}$, shaded by fraction of kinetic energy due to waves; and (d) shows ripple wavelength, λ. The vertical dashed lines in panel (d) indicate occurrences of local bathymetries shown as panels (e)–(j). Panels (e)–(j) show 2-D bathymetries, where y is shore parallel and x is shore normal, with $-x$ directed onshore, and is shaded by bedform height. Finally, dashed lines and shaded overlay in e–j indicate bedform orientation and orientation uncertainty, respectively.

time at S1 and S2, wave dominant flows occurred 52% of the time at S1 and 67% of the time at S2, and combined wave-current flows occurred 46% of the time at S1 and 33% at S2. During nonstorm conditions semidiurnal peaks in the energy were associated with the tide as evident with low $E_{k_w}/E_{k_{wc}}$. At S2 larger wavelength bedforms corresponded with instances of increased flow and occurred generally under current or combined flow dominant kinetic energy. However, observations at S1 showed that relatively large wavelength bedforms ($\lambda > 1$ m) can correspond with instances of large kinetic energy that was either current dominated or high wave energy-dominated conditions (i.e., storms). Additionally, bedform steepness was generally characteristic of wave orbital ripple steepness ($\eta/\lambda \approx 0.16$) during wave energy-dominated conditions, and dune steepness ($\eta/\lambda \approx 0.06$) during current energy-dominated conditions (Fredsøe & Deigaard, 1992; Wiberg & Harris, 1994). Figure 4 shows a truncated time series from Figure 2 to highlight the growth of one bedform over time with corresponding sonar images to show bed change.

3.2. Bedform Characterization

The distribution of the relative frequency of occurrence during each deployment of λ, η, and η/λ (Figures 5a–5c for each site S1 and S2) shows that smaller wavelength bedforms occurred more often, and generally bedforms were in the range of the steepness of wave orbital ripples ($\eta/\lambda \approx 0.16$). However, the histogram of λ also shows that at each site bedforms of wavelengths longer than 0.5 m occurred between 29% and 33% of the time, and bedforms with a steepness of less than that of wave orbital ripples occur approximately 29–35% of the time. The observed bedforms were predominantly 2-D, but during transition periods, bedforms could become 3-D; the degree of three dimensionality is shown through the observed spread of dominant bedform orientation, as indicated with a shaded gray band (Figure 4).

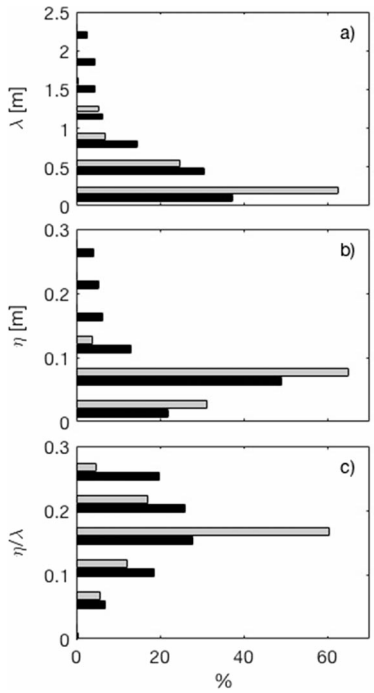

Figure 5. Histograms of bedform (a) wavelength (λ), (b) amplitude (η), and (c) steepness (η/λ) at both stations, where S1 is in black and S2 is in gray.

Ripples observed in wave-dominated environments are often characterized as either orbital ripples, suborbital ripples, and anorbital ripples (Clifton & Dingler, 1984; Wiberg & Harris, 1994). The wavelength of orbital ripples scales with the orbital excursion of the waves. Anorbital ripples have a wavelength independent of orbital excursion and are thought to scale with the grain size. Suborbital ripples are some combination of the two regimes (Clifton & Dingler, 1984; Wiberg & Harris, 1994). The Clifton and Dingler (1984) classification diagram is shown in Figure 6a overlaid with observations from S1 and S2. The wave-dominated bedforms, with large $E_{k_w}/E_{k_{wc}}$, generally were classified as orbital or slightly suborbital (falling on the dark gray bar in Figure 6a and are consistent with Clifton and Dingler ; 1984). However, ripples with larger wavelengths correspond to periods with smaller $E_{k_w}/E_{k_{wc}}$ (Figure 6a, blue shading) and fall in an unclassified region in Clifton and Dingler (1984). The unclassified bedforms did not show evidence of being relic (Figure 6a). Considering such attributes, we consider the bedforms that fall into this unclassified region by Clifton and Dingler (1984) as either combined wave-current or current dominant bedforms and were formed by the onset of strong currents.

Figure 6b shows the distribution of observed bedform wavelength as a function of $E_{k_w}/E_{k_{wc}}$, u_o, and U for both S1 and S2 sites. S1 and S2 were influenced strongly by tidal currents particularly with the occurrence of large U at relatively small u_o; that is, when wave-driven alongshore currents were weak (see Hay & Mudg, 2005, Figure 11, for a reference case with small tidal currents). Additionally, larger wavelength bedforms were shown to occur with large u_o and/or large U, indicating that bedforms may have been formed by waves, currents, and with combined wave-current forcing contributions, shown by the shading of $E_{k_w}/E_{k_{wc}}$.

3.3. Observations of Bedform Orientation

The bedforms at S1 and S2 were very dynamic. During transitional periods they were not aligned and instead were oriented over a range of directions between 5° and 90°. The bandwidth range was determined by the spacing between peaks in 2-D spatial spectra and is indicated by a shaded gray band in Figure 7 and a shaded gray band on each 2-D bathymetry plot (Figures 2–4). The bedforms generally did not align with the current or the wave direction, but rather a combination of both depending on flow dominance. The bedforms sometimes align with the wave direction when $E_{k_w}/E_{k_{wc}}$ was large, notably during low tide, and with the current direction when $E_{k_w}/E_{k_{wc}}$ was small (Figures 7b and 7c). However, the bedforms did not always align with the dominant flow direction (e.g., Figures 7b and 7c, day of year 281.2).

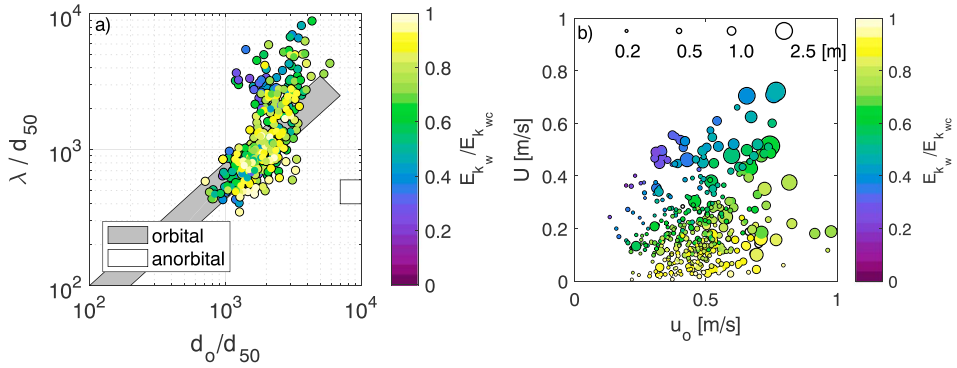

Figure 6. Bedform classification scatter plot diagrams. Panel (a) shows the Clifton and Dingler (1984) classification diagram (dark gray are classified as orbital ripples and white as anorbital ripples, with the region in between classified as suborbital ripples) overlaid with observations from S1 and S2, shaded by fraction of kinetic energy due to waves. Panel (b) shows the distribution of observed bedform wavelengths based on orbital velocity and current velocity flow contributions, shaded by fraction of energy due to waves, where the marker size indicates bedform wavelength (with larger markers indicating larger λ as shown at the top of the panel).

Figure 8 shows the bedform orientation in relation to the current magnitude and direction, the wave orbital magnitude and direction, the bedform wavelength, and $E_{k_w}/E_{k_{wc}}$. When considering the bedform orientation in relation to the current and wave directions (Figures 8a and 8d), the bedforms generally did not align with either the current or wave direction. The strongest correlation between the four metrics displayed is the bedform orientation in relation to the current magnitude (Figures 8b and 8e). As bedforms became more current influenced (low $E_{k_w}/E_{k_{wc}}$) they not only increased in wavelength but also tended to orient between 30° and 70°, approaching the direction of the prevailing flood tidal currents oriented toward the northeast (90° counterclockwise from shore normal in Figure 1). Figure 8c shows the difference between the bedform orientation and the current direction, with greater influence from the currents, the difference between the bedform orientation and current direction decreased. The bedform orientation in relation to the orbital velocity magnitude did not show as clear of a trend (Figure 8e); however, Figure 8f shows that as the wave orbital velocity magnitude increased, the difference between the wave direction and the bedform orientation decreased, showing that the wave orbital velocity magnitude did influence the bedform orientation.

A root-mean-square error range ($rmse_{\text{range}}$) analysis is used to determine how well the bedform orientation observations fit the wave and current directions. The metric is a modified *rmse* calculation, where the difference between the measured and modeled orientations are set to 0 if the wave or current direction falls anywhere within the bedform orientation bandwidth range, and the differences are calculated at the center of the range if the wave or current direction falls outside. Circular statistics were used to calculate the root-mean-square-error range. The bedform orientation root-mean-square error range statistics (given in the caption of Figure 8) show that the bedform orientation was neither predominantly influenced by waves or currents. However, with respect to the root-mean-square error range analysis, the bedforms were more closely aligned with the wave direction than the current direction. Overall, the generally large root-mean-square error range values indicate that the bedform orientation was not a function of the independent wave and current directions alone, but rather a concurrent combination (Gallagher et al., 1998; Lacy et al., 2007).

4. Discussion

4.1. Time-Evolving Bedform Geometry and the Sediment Continuity Equation

Observations show that bedforms can grow/decay and not migrate, migrate and not grow/decay, or do some combination of both growing/decaying and migrating. The relationship between hydrodynamic forcing and bedform wavelength growth over one tidal cycle is shown in Figure 4. In combined wave-current flows, the bedform wavelength increased with increasing duration of forcing demonstrating that λ at any instance in time was dependent not only on present hydrodynamic forcing but also on past hydrodynamic conditions over some lag time, τ. From (19) the estimated change in bedform volume is shown to depend on q_b—estimated from either (14) or (15) with similar magnitudes (Figure 9e), the bedform geometry, the nondimensional phase shift between the assumed sinusoidal bedform shape and sinusoidal transport curve

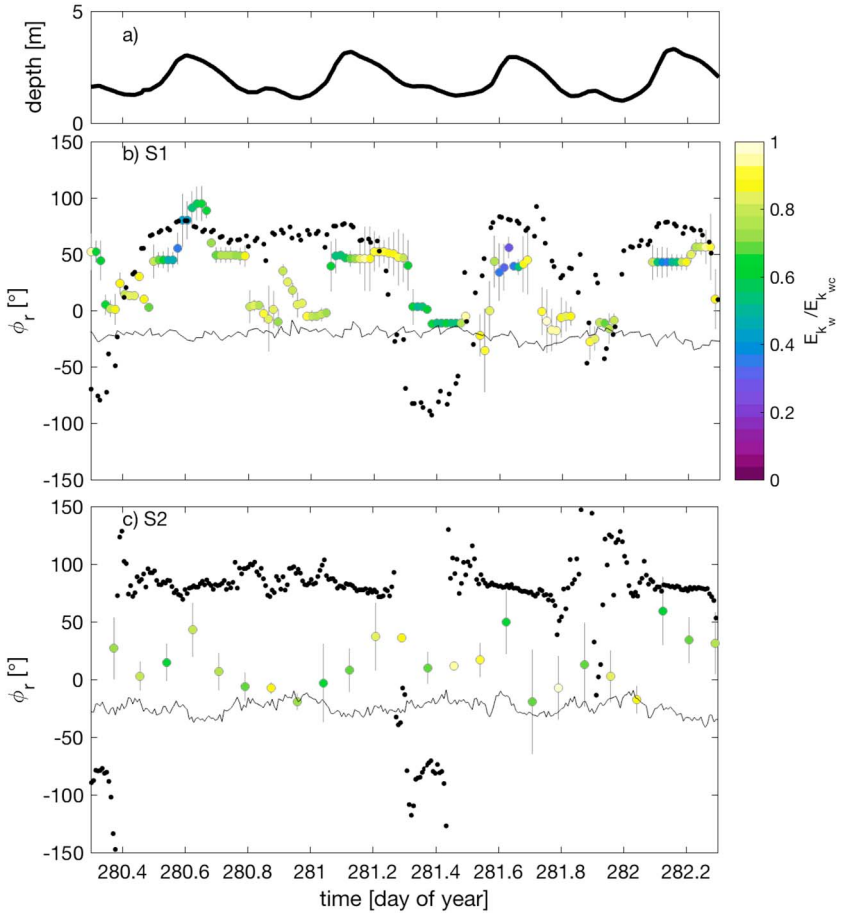

Figure 7. Observed bedform direction and concurrent flow directions. Panel (a) shows a time series of depth at S1. Panels (b) S1 and (c) S2 show time series of range of observed bedform orientation colored by fraction of kinetic energy due to waves (circles with range bars), observed current direction (black dots), and observed wave direction (thin black line).

(δ_{x_b}/λ), and the time lag for bedform growth (τ). The significance of the nondimensional phase shift and time lag for growth are further discussed in the following paragraphs.

The bedform will grow/decay and/or migrate with dependence on the x position of peak transport with respect to the bedform crest position. Physically, during bedform growth $d\eta/dt$ is observed to be large, and the bedform is observed to grow but not migrate if the 2-D cross correlation or MEP used to estimate the bedform migration rate have a low-magnitude peak correlation and a peak offset of 0, indicating that the bedform has changed shape (low correlation) and that the bedform did not move (zero-peak offset). Analytically, the differentiation between bedform growth/decay and migration is described with a phase shift between the peak position in the transport over the bedform and the position of the bedform crest as described with the nondimensional phase shift, δ_{x_b}/λ. The δ_{x_b}/λ was estimated using (17) by taking $t = \mathrm{d}t$ and $x = 0$ since the nondimensional phase shift is estimated with every measurement of bedform growth or decay and is estimated in x position along the bedform with respect to the bedform crest (at $x = 0$). With the onset of increased $E_{k_{wc}}$, the bedform can grow and/or migrate; when the bedform growth dominates, δ_{x_b}/λ will be close to +0.25; when the bedform decay dominates, δ_{x_b}/λ will be close to −0.25; and when bedform migration dominates, δ_{x_b}/λ will be close to 0 (Figures 9 and 10; Nielsen, 1992). Generally, the largest periods of bedform growth or decay have small migrations, and the largest periods of migration have small growth or decay (Figure 10). The sediment transport increases with either increased migration or increased growth, and decays with decreased migration or bedform decay.

Three methods are used to estimate the lag time for bedform growth, τ. The first method assumes that τ does not change with time, the second estimates τ based upon observations of bedform growth and decay, and

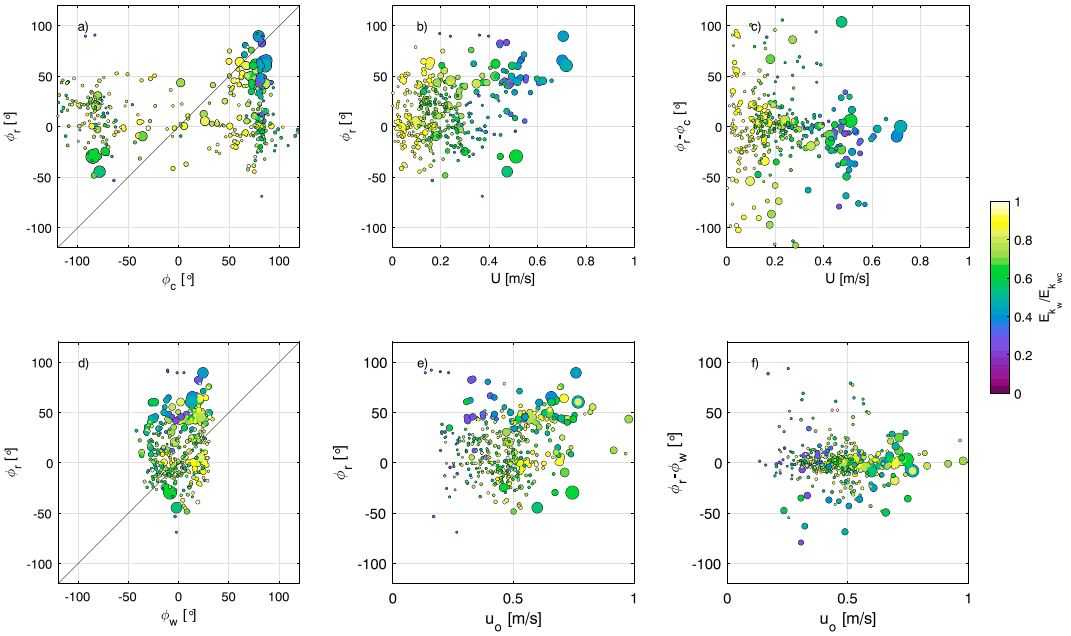

Figure 8. Observed bedform directions plotted against (a) current direction ($rmse_{range}$ = 40°), (b) current magnitude, (d) wave orbital direction ($rmse_{range}$ = 23°), and (e) wave orbital magnitude. And difference between observed bedform orientation and prevailing current/wave direction plotted against (c) current magnitude for current direction and (f) wave orbital velocity magnitude for wave direction. *rmse* is calculated between the observed bedform range and the model as described in the text. Markers are colored by the fraction kinetic of energy due to waves and the size of the marker scales with the bedform wavelength as indicated in Figure 6b.

the third evaluates an existing method to approximate τ. The first method sets $\tau = dt$, one sample time step (for S1 dt = 20 min, and for S2 dt = 2 hr). The second method sets $\tau = \tau_{zc}$, or the adjustment time found with observations of bedform growth or decay by the time between subsequent upward and downward zero crossings in $d\Lambda_b/dt$. An upward zero crossing indicates the initiation of bedform growth, and a downward zero crossing indicates the start of bedform decay. The time between upward to downward zero crossings represents the adjustment time that the bedform underwent to reach its largest volume before it started to decay. The time between downward to upward zero crossings represents the adjustment time for bedform decay. Depending upon the flow forcing condition, τ_{zc} will change. If the bedform reaches an equilibrium condition with the flow and stops growing or decaying, the lag time was set to dt. An example of an individual bedform growing over time at S1 is shown in Figure 4. In this case the bedform adjusted to the flow field for approximately 2.4 hr (0.1 days) before its volume began to decay; thus, for this case τ_{zc} = 2.4 hr. The observed bedform adjustment time using the zero-crossing method showed that within wave dominant conditions, the bedform adjustment time was fairly quick. Within 20 min to 1 hr the bedforms began to come into equilibrium with the flow field; however, with the addition of currents, the adjustment time became much longer, approximately 2.5 to 6 hr and the bedforms may have never adjusted into equilibrium with the flow forcing. The third method to find τ uses $\tau = \frac{n\eta\lambda}{2q_b}$ (Traykovski, 2007). The method assumes that the sediment flux during bedform growth is uniform with respect to time. Since (19) estimates the change in bedform volume as a function of the sediment transport, it is viable even through quiescent conditions. However, with the dynamic qualities of this data set, has not been evaluated in a quiescent environment. At S1, τ was estimated using the all three methods. However, at S2, the bedform zero-crossing method could not be used because the sampling rate between subsequent sonar images was too slow to capture bedform building.

The results of the continuity analysis given by (19) are shown as Figures 11 and 12. The bedform volume, Λ_b, was measured by taking the average cross section of the ripple profile in the direction of the bedform orientation divided by the measured ripple wavelength from the 2-D spectra to find the mean bedform volume for each time step. The measured change in bedform volume, $\Delta\Lambda_b$, was then calculated by subtracting subsequent bedform volume measurements. The estimated $\Delta\Lambda_b$ was found with (19) over the period of growth or

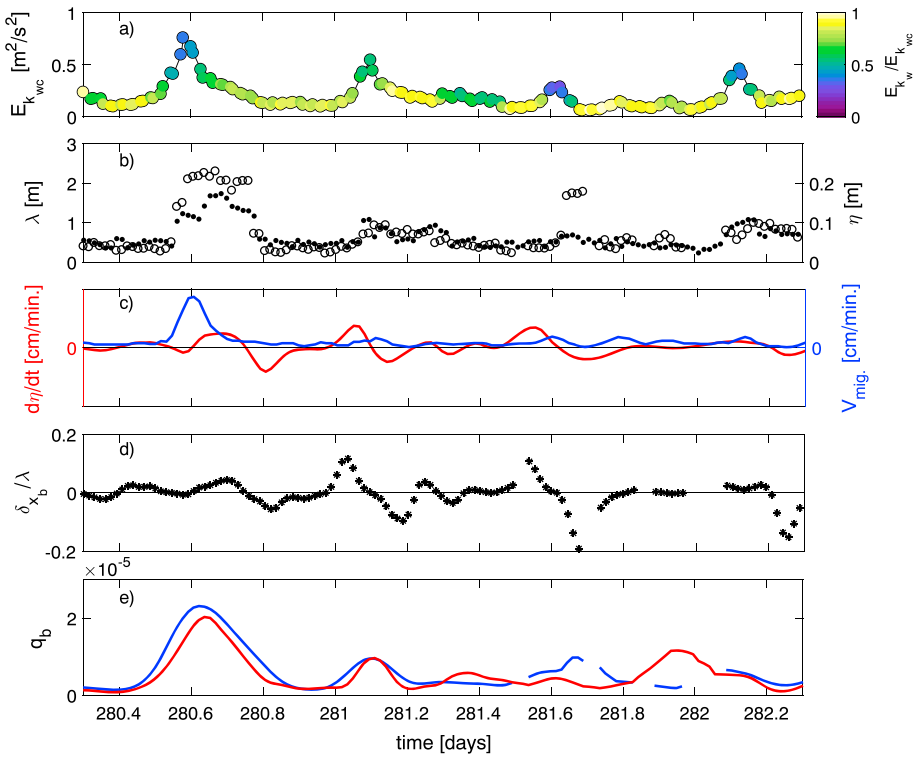

Figure 9. Time series of indicators for bedform growth, decay, and migration. Panel (a) shows the wave-current energy time series colored by fraction of kinetic energy due to waves at S1. Panel (b) shows a short time series of bedform wave length (o) and height (•). Panel (c) shows the bedform growth/decay rate in red and the bedform migration rate in blue. Panel (d) shows the nondimensional phase offset between the sediment transport and bed shape, when δ_{x_b}/λ is positive the bedform will grow, negative will decay, and 0 will migrate. Panel (e) shows the bedload sediment transport estimated with equations (14) (blue) and (15) (red).

decay expressed with the integral of the sediment flux over $t-\tau$ to t. Observations captured many instances of bedform building and decay over time (e.g., Figure 4). When $\tau = dt$, (19) greatly underestimates the change in bedform volume, especially for S1 where dt is much shorter (Figures 11 and 12). The underestimation is especially apparent during instances of increased changes in bedform volume, suggesting that bedform building or decay is a time-dependent process. At both S1 and S2, it is clearly evident that (19) has higher skill using a variable τ (second and third methods). Figures 11b and 12 demonstrate that τ estimated directly from the bedform zero-crossing method ($rmse = 0.019$ m^3/m, $r^2 = 0.86$ for S1) or calculated using $\tau = \frac{n\eta\lambda}{2q_b}$ ($rmse = 0.021$ m^3/m, $r^2 = 0.64$ for S1 and S2) represents the range of measured bedform volumes much better than $\tau = dt$ ($rmse = 0.029$ m^3/m, $r^2 = 0.22$ for S1 and S2).

4.2. Existing Time-Dependent Bedform Geometry Model Comparisons

Previous bedform geometry work primarily focuses on approximating bedform geometry (λ and η) from the overlying flow field; however, in our effort bedform volume (Λ_b) was instead estimated with the sediment continuity equation (presented in the previous section). The leading time-dependent bedform geometry models for prediction of bedform wavelength and height are Traykovski (2007) and Soulsby et al. (2012). Each model was evaluated using the data collected at S1 and S2 for all flow conditions as well as a subset of the data that represents conditions for which the model was developed (Figure 13).

The Traykovski (2007) model was unable to predict occurrences of combined flow bedforms with high skill. However, the model is formulated for waves only; when applied to only wave dominant conditions, it was able to successfully predict the geometry of smaller orbital ripples with a twofold increase in the r^2 and a two-thirds reduction in *rmse* for both predictions of λ and η when compared to the prediction for all flow conditions observed (Figures 13a and 13c). Wave dominant ripples are considered to be when $E_{k_w}/E_{k_{wc}} > 0.75$,

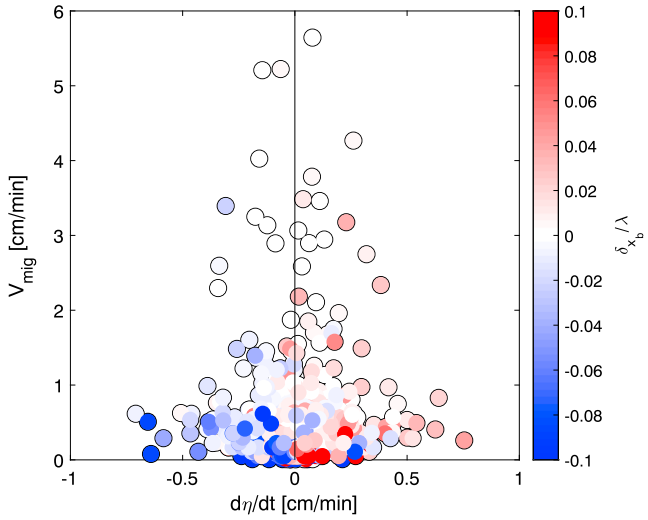

Figure 10. Scatter plot of bedform growth/decay and migration rate, colored by the nondimensional phase offset between the sediment transport and bed shape, δ_{x_b}/λ is estimated with (17). When δ_{x_b}/λ is positive, the bedform will grow, negative will decay, and 0 will migrate.

and the model is suitable for predicting bedform geometry in those conditions. Although the model did not predict bedform geometry in combined flows well, the concept behind the adjustment time scale, T_{adj}, in the Traykovski (2007) model is valid for both wave and current generated bedforms (as shown in Figure 12).

The Soulsby et al. (2012) model is applicable to either wave- or current-generated bedforms, but it generally fails to predict megaripple scale bedforms. The model was calibrated for bedforms with wavelengths of 0.5 m

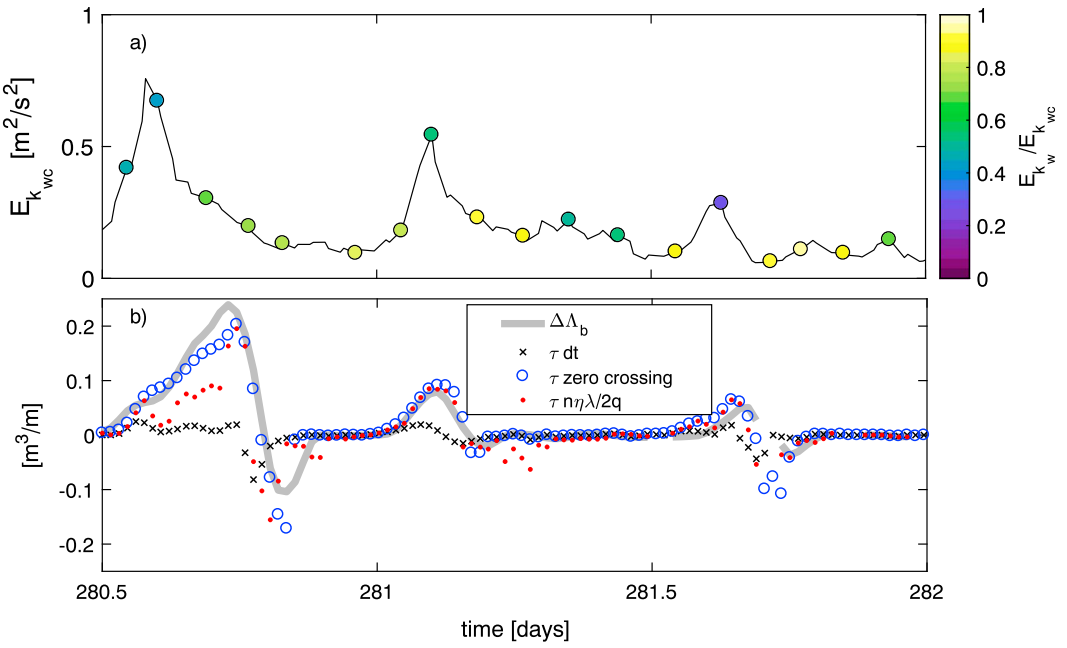

Figure 11. Time series of bedform volume represented by the sediment continuity equation. Panel (a) shows the wave-current energy time series colored by fraction of kinetic energy due to waves at S1. Panel (b) shows a short time series of $\Delta\Lambda_b$, where the thick gray line is the measured change in bedform volume from (19) and the markers represent the estimated change from (19) over the lag time for growth/decay, τ. The τ is estimated as follows: the black × use a $\tau = dt$, the blue ◦ use a τ directly estimated from the bedform zero-crossing method, and the red • use a τ estimated from ($\tau = \frac{n\eta\lambda}{2q_b}$).

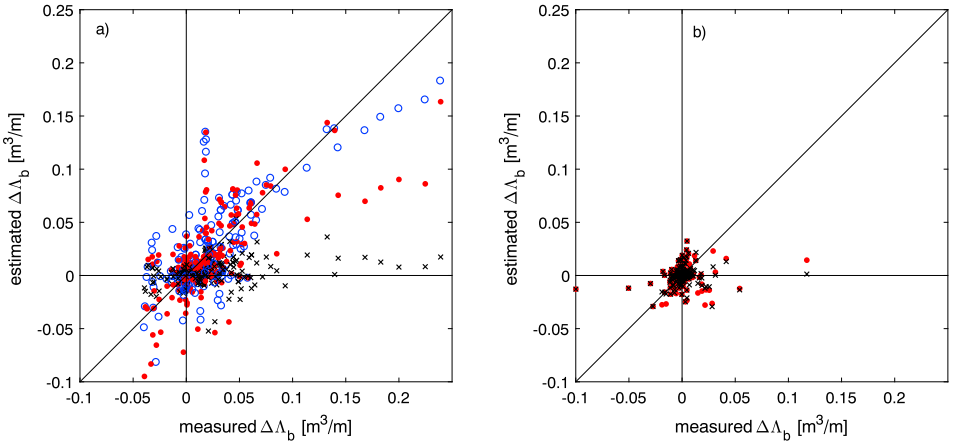

Figure 12. Scatter plot of the change in bedform unit volume (measured) versus the time-integrated transport (estimated) from (19) for the full data set collected at (a) S1 and (b) S2. The change in bedform volume (x axis) is plotted against the time-integrated sediment flux using different approximations of the bedform lag time, τ (y axis). The black × use a $\tau = \mathrm{d}t$, the blue ∘ use a τ directly estimated from the bedform zero-crossing method, and the red • use a τ estimated from ($\tau = \frac{n\eta\lambda}{2q_b}$). The solid black line is a 1 to 1 line. For the bedform zero-crossing method, *rmse* = 0.019 m^3/m, r^2 = 0.86 for S1. For $\tau = \frac{n\eta\lambda}{2q_b}$, *rmse* = 0.021 m^3/m, r^2 = 0.64. For $\tau = \mathrm{d}t$, *rmse* = 0.029 m^3/m, r^2 = 0.22.

or less (see Figure 5 for distribution of bedform wavelengths observed), if the model is used to predict bedforms with only wavelengths less than 0.5 m, the model r^2 stayed the same, but the model *rmse* decreased by two thirds or more regardless of flow dominance, suggesting a model bias. The Soulsby et al. (2012) model may poorly predict larger volume bedforms for several reasons; first, the model excludes the effects of combined flows that are prevalent at S1 and S2.The model estimates of the equilibrium bedform geometry considerably underpredict λ_{eq}(~ 0.3 m) compared with observed bedform wavelengths (λ = 1–2.5 m) during combined flows. The criterion distinguishing between wave or current generated bedforms is based on the Shields parameter, and depending on the approximation used for bed stress, the Shields parameter may underpredict mobility during combined flow conditions at the S1 and S2 sites. Finally, the transition from wave-generated to current-generated bedforms in the Soulsby et al. (2012) model is abrupt and does not allow for combined flow bedform generation.

Although the adjustment characteristic toward an equilibrium length scale in Traykovski (2007) and Soulsby et al. (2012) seems reasonable, in practice, dependence on an equilibrium length scale may hinder the model skill (especially during combined flow conditions). In our data set, although wave-dominated bedforms at times come into equilibrium with the wave conditions, the combined flow bedforms never actually came into equilibrium with the flow forcing. The time series of bedform wavelength in comparison with the time series of the flow kinetic energy in Figures 2–4 and 9 provide evidence for combined flow bedforms not reaching equilibrium in our data. If bedforms had reached equilibrium during the combined flow conditions, the bedform wavelength would have reached a constant with consistent combined flow kinetic energy forcing, which was not observed. Present equilibrium theory may not be representative of the physics of combined flow bedform growth; it may be that combined flow bedforms have a longer equilibrium time that is dependent on hydrodynamic conditions as well as water depth. Even with the limitations of the Traykovski (2007) and Soulsby et al. (2012) models, their incorporation of time-dependent growth is relevant to bedform building, even in combined wave-current flows. Other models that attempt to predict bedform wavelengths and heights that do not incorporate a growth time dependence were evaluated (not shown) and have an *rmse* of 0.6 m or greater for bedform wavelength and 0.05 m or greater for bedform height, which is a larger *rmse* than both time-dependent models evaluated even when for conditions that the models were not calibrated (including ; Li & Amos, 1998; Nelson et al., 2013; Nielsen, 1981; Soulsby & Clarke, 2005; Testik et al., 2005; Wiberg & Harris, 1994; Wikramanayake & Madsen, 1994), again, showing the importance of the time of exposure to bedform growth and decay.

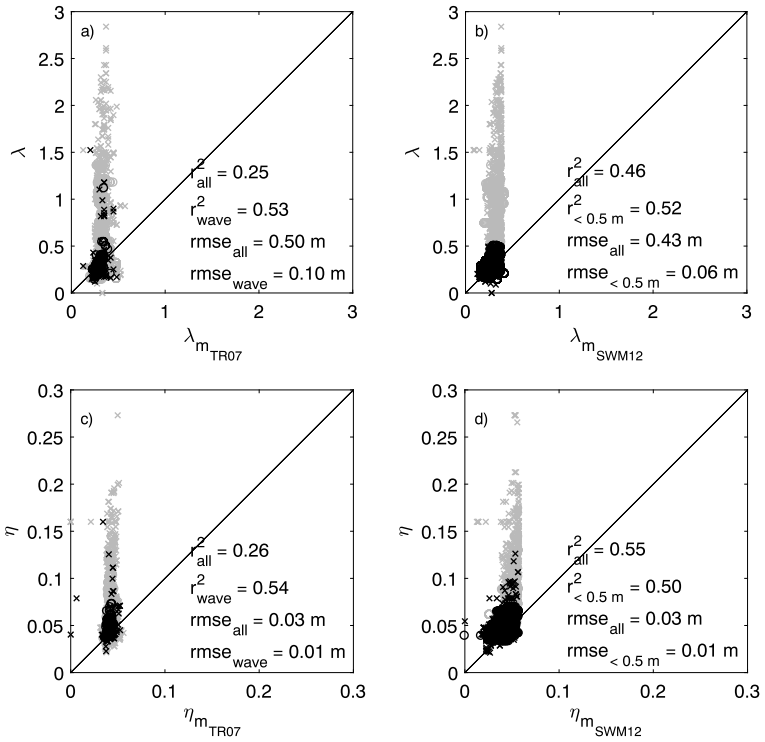

Figure 13. Observed versus modeled bedform λ (panels a and b) and η (panels c and d) for site S1 in × and S2 in ∘. The gray markers show all data, and the black markers show the subset of data that the model was designed and tested on. Panels (a) and (c) plot the Traykovski (2007) model from (20), where the data in black are for wave dominant flows only; panels (b) and (d) plot the Soulsby et al. (2012) model from (21), where the data in black are for bedforms less than 0.5 m in wavelength only. The model *rmse* and r^2 are indicted in the lower right corner of each panel.

5. Conclusions

Observations of bedform response to wave, current, and high-energy combined wave-current dominant flows are presented. The observations capture both ripple and megaripple response to hydrodynamic conditions consisting of wave forcing plus strong currents (>0.5 m/s) collected within and near the surf zone. Dynamic bedform geometry transitions in response to shifts in flow conditions are resolved. Observations show that bedform volume—when exposed to current and combined wave-current forcing—continuously build until the flow changes.

Bedform transformation and growth are shown to be a highly time dependent sediment transport process. With hydrodynamic transitions, the bedform scaling did not respond immediately; instead, the bedform adjustment lagged behind in response to new forcing condition. Within wave dominant conditions, the bedform adjustment time was fairly quick; within 20 min to 1 hr the bedforms began to come into equilibrium with the flow field. However, when strong currents were present, the adjustment time became much longer, ranging between 2.5 and 6 hr and the bedforms never actually came into complete equilibrium with the flow forcing. The departure from equilibrium conditions captured in this data set may be responsible for the inability of existing bedform geometry models to predict bedform wavelength and height in the measured combined flows. Demonstrating that current equilibrium theory may not be representative of combined flow bedform growth or, at least not consistent with the stability condition for combined wave-current bedforms.

Aside from our dynamic set of observations of bedform response to combined wave-current flows, our effort demonstrates that bedform volume at any given time was dependent on both the sediment transport rate and the time duration that the bedform was exposed to the flow field. Measured changes in bedform volume were additionally shown to be characterized with the sediment continuity equation, or Exner equation, integrated over the bedform adjustment time of growth, which to our knowledge is a new contribution that builds upon past efforts. In addition, our effort contributes expressions for the fully unsteady bedform migration rate, growth rate, sediment transport phase shift, and change in volume. The sediment continuity equation

while accounting for bedform adjustment/growth times may be a viable method for temporal and spacial morphologic change predictions of bedforms, especially in combined wave-current flows and with bedforms of a larger scale.

Acknowledgments
We would like to acknowledge the team of graduate students, faculty members, and technicians, from multiple countries and institutions, who helped collect these data, with special thanks to Jon Hunt from UNH. We would especially like to thank Dano Roelvink, who significantly contributed to the theoretical development behind this work, as well as the thoughtful comments of an anonymous reviewer. Additionally, we would like to thank the many departments and foundations who funded in this work. MegaPEX was funded through NWO grant 12686, Nature Coast, and ERC Advance grant 91206, NEMO. The UNH contribution to MegaPEX was funded by the PADI Foundation. M. E. W. was supported by the U.S. Department of Defense NDSEG fellowship. D. L. F. was funded by NSF grant 1135026. T. C. L. was funded under ONR contract N00014-14-1-0557. M. d.S. was supported by NWO grant 15058, Feeding Starved Coasts by Morphological Diffusivity. J. C. was supported under base funding to the U.S. Naval Research Laboratory from the Office of Naval Research. Data from MegaPEX can be found at data.4tu.nl/repository/collection:zandmotor

References

Alamo, J. C., & Jimenez, J. (2003). Spectra of very large anisotropic scales in turbulent channels. *Physics of Fluids Letters*, *15*(6), L41–L44.
Austin, M. J., Masselink, G., O'Hare, T. J., & Russell, P. E. (2007). Relaxation time effects of wave ripples on tidal beaches. *Geophysical Research Letters*, *34*, L16606. https://doi.org/10.1029/2007GL030696
Becker, J. M., Firing, Y. L., Aucan, J., Holman, R., Merrifield, M., & Pawlak, G. (2007). Video-based observations of nearshore sand ripples and ripple migration. *Journal of Geophysical Research*, *112*, C01007. https://doi.org/10.1029/2005JC003451
Clifton, H. E., & Dingler, J. R. (1984). Wave-formed structures and paleoenvironmental reconstruction. *Marine Geology*, *60*, 165–198.
Davis, J. P., Walker, D. J., Townsend, M., & Young, I. R. (2004). Wave-formed sediment ripples: Transient analysis of ripple spectral development. *Journal of Geophysical Research*, *109*, C07020. https://doi.org/10.1029/2004JC002307
Doucette, J. S., & O'Donoghue, T. (2006). Response of sand ripples to change in oscillatory flow. *Sedimentology*, *53*, 581–596.
Fredsøe, J. (1984). Turbulent boundary layer in wave-current motion. *Journal of Hydraulic Engineering*, *110*(8), 1103–1120.
Fredsøe, J., & Deigaard, R. (1992). *Mechanics of coastal sediment transport*. Singapore: World Scientific.
Gallagher, E. L. (2003). A note on megaripples in the surf zone: Evidence for their relation to ready flow dunes. *Marine Geology*, *193*, 171–176.
Gallagher, E. L., Elgar, S., & Thornton, E. B. (1998). Megaripple migration in a natural surf zone. *Letters to Nature*, *394*, 165–168.
Ganju, N. E., & Sherwood, C. R. (2010). Effect of roughness formulation on the performance of a coupled wave, hydrodynamic, and sediment transport model. *Ocean Modeling*, *33*, 299–313.
Grant, W. D., & Madsen, O. S. (1979). Combined wave and current interaction with a rough bottom. *Journal of Geophysical Research*, *84*(C4), 1797–1808.
Hay, A. E., & Mudg, T. (2005). Principal bed states during sandyduck97: Occurrence, spectral anisotropy, and the bed state storm cycle. *Journal of Geophysical Research*, *110*, C03013. https://doi.org/10.1029/2004JC002451
Lacy, J. R., Rubin, D. M., Ikeda, H., Mokudai, K., & Hanes, D. M. (2007). Bed forms created by simulated waves and currents in a large flume. *Journal of Geophysical Research*, *112*, C10018. https://doi.org/10.1029/2006JC003942
Larsen, S. M., Greenwood, B., & Aagaard, R. (2015). Observations of megaripples in the surf zone. *Marine Geology*, *364*, 1–11.
Lesser, G. R., Roelvink, J. A., van Kester, T. M., & Stelling, G. S. (2004). Development and validation of a three-dimensional morphological model. *Coastal Engineering*, *51*, 883–915.
Li, M. Z., & Amos, C. L. (1998). Predicting ripple geometry and bed roughness under combined waves and currents in a continental shelf environment. *Continental Shelf Research*, *18*, 941–970.
Madsen, O., Poon, Y., & Graber, H. (1988). Spectral wave attenuation by bottom friction: Theory. In *Coastal Engineering, Proceedings of the 21st Conference Am. Soc. Civ. Eng. New York, 1* (pp. 492–504). New York.
Maier, I., & Hay, A. (2009). Occurrence and orientation of anorbital ripples in near-shore sands. *Journal of Geophysical Research*, *114*, F04022. https://doi.org/10.1029/2008/JF001,126
Meyer-Peter, E., & Muller, R. (1948). Formulas for bed-load transport, *Report on the second meeting of the International Association for Hydraulic Structures Research* (pp. 39–64). Stockholm.
Nelson, T. R., & Voulgaris, G. (2015). A spectral model for estimating temporal and spatial evolution of rippled seabeds. *Ocean Dynamics*, *65*, 155–171.
Nelson, T. R., Voulgaris, G., & Traykovski, P. (2013). Predicting wave-induced ripple equilibrium geometry. *Journal of Geophysical Research: Oceans*, *118*, 3202–3220. https://doi.org/10.1002/jgrc.20241
Nielsen, P. (1981). Dynamics and geometry of wave-generated ripples. *Journal of Geophysical Research*, *86*(C7), 6467–6472.
Nielsen, P. (1992). *Coastal bottom boundary layers and sediment transport*. Singapore: World Scientific.
Passchier, S., & Kleinhans, M. G. (2005). Observations of sand waves, megaripples, and hummocks in the Dutch coastal area and their relation to currents and combined flow conditions. *Journal of Geophysical Research*, *110*, F04S15. https://doi.org/10.1029/2004JF000215
Penko, A., Calantoni, J., & Hefner, B. T. (2017). Modeling and observations of sand ripple formation and evolution during TREX13. *Journal of Oceanic Engineering*, *42*, 260–267.
Perkovic, D., Lippmann, T., & Frasier, S. (2009). Longshore surface currents measured by doppler radar and video PIV techniques. *IEEE Transactions on Geoscience and Remote Sensing*, *47*(8), 2787–2800. https://doi.org/10.1109/TGRS.2009.2016556
Radermacher, M., de Schipper, M. A., Swinkels, C., MacMahan, J. H., & Reniers, A. J. (2017). Tidal flow separation at protruding beach nourishments. *Journal of Geophysical Research: Oceans*, *122*, 63–79. https://doi.org/10.1002/2016JC011942
Roelvink, D., & Reniers, A. J. H. M. (2011). *A guide to modeling coastal morphology* (Vol. 12). Singapore: WSPC.
SeaBeam (2000). Multibeam sonar theory of operation (*Tech. Rep.*): L3 Communications of SeaBeam Instruments.
Smith, D., & Sleath, J. F. A. (2005). Transient ripples in oscillatory flows. *Continental Shelf Research*, *25*, 485–501.
Soulsby, R., & Clarke, S. (2005). Bed shear-stresses under combined waves and currents on smooth and rough beds (*Report TR 137*). Wallingford, UK: HR Wallingford.
Soulsby, R. L., Whitehouse, R. J. S., & Marten, K. V. (2012). Prediction of time-evolving sand ripples in shelf seas. *Continental Shelf Research*, *38*, 47–62.
Stive, M. J. F., de Schipper, M. A., Luijendijk, A. P., Aarninkhof, S. G. J., van Gelder-Maas, C., van Thiel de Vries, J. S. M., et al. (2013). A new alternative to saving our beaches from sea-level rise: The sand engine. *Journal of Coastal Research*, *29*(5), 1001–1008.
Testik, F. Y., Voropayev, S. I., & Fernando, H. J. S. (2005). Adjustment of sand ripples under changing water waves. *Physics of Fluids*, *17*, 072104.
Traykovski, P. (2007). Observations of wave orbital scale ripples and a nonequilibrium time-dependent model. *Journal of Geophysical Research*, *112*, C06026. https://doi.org/10.1029/2006JC003811
Traykovski, P., Hay, A. E., Irish, J. D., & Lynch, J. F. (1999). Geometry, migration, and evolution of wave orbital ripples at LEO-15. *Journal of Geophysical Research*, *104*(C1), 1505–1524.
Wengrove, M. E., Foster, D. L., de Schipper, M. A., & Lippmann, T. C. (2017). Wave and current ripple formation and migration during storms. *Proceedings of Coastal Dynamics*, *2017*(129), 955–965.
Wiberg, P. L., & Harris, C. K. (1994). Ripple geometry in wave-dominated environments. *Journal of Geophysical Research*, *99*, 775–789.
Wikramanayake, P. N., & Madsen, O. S. (1994). Calculation of movable bed friction factors (*Technical report for us army corps of engineers*). Boston, MA: Massachusetts Institute of Technology.